Journal Pre-proofs

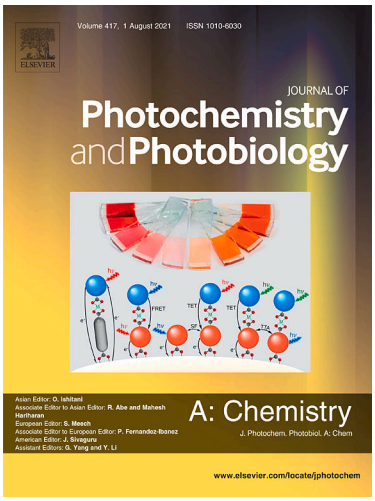

Enhancing the electrical, optical, and structure morphology using Pr_2O_3-ZnO nanocomposites: Towards electronic varistors and environmental photocatalytic activity

T.H. AlAbdulaal, M. AlShadidi, Mai S.A. Hussien, G. Vanga, A. Bouzidi, Saqib Rafique, H. Algarni, H.Y. Zahran, M.Sh. Abdel-wahab, I.S. Yahia

PII: S1010-6030(21)00270-7
DOI: https://doi.org/10.1016/j.jphotochem.2021.113399
Reference: JPC 113399

To appear in: *Journal of Photochemistry & Photobiology, A: Chemistry*

Received Date: 11 March 2021
Revised Date: 21 May 2021
Accepted Date: 29 May 2021

Please cite this article as: T.H. AlAbdulaal, M. AlShadidi, M.S.A. Hussien, G. Vanga, A. Bouzidi, S. Rafique, H. Algarni, H.Y. Zahran, M.Sh. Abdel-wahab, I.S. Yahia, Enhancing the electrical, optical, and structure morphology using Pr_2O_3-ZnO nanocomposites: Towards electronic varistors and environmental photocatalytic activity, *Journal of Photochemistry & Photobiology, A: Chemistry* (2021), doi: https://doi.org/10.1016/j.jphotochem.2021.113399

Enhancing the electrical, optical, and structure morphology using Pr_2O_3-ZnO nanocomposites: Towards electronic varistors and environmental photocatalytic activity

T.H. AlAbdulaal[1*], M. AlShadidi[1], Mai S. A. Hussien[2,3], G. Vanga[1], A. Bouzidi[4], Saqib Rafique[5], H. Algarni[1], H.Y. Zahran[1,3], M.Sh. Abdel-wahab[6], I.S. Yahia[1,3,7]

[1]*Department of Physics, Faculty of Science, King Khalid University, P.O. Box 9004, Abha, Saudi Arabia*

[2]*Department of Chemistry, Faculty of Education, Ain Shams University, Roxy, 11757 Cairo, Egypt.*

[3]*Nanoscience Laboratory for Environmental and Bio-medical Applications (NLEBA), Semiconductor Lab., Metallurgical Lab.1. Department of Physics, Faculty of Education, Ain Shams University, Roxy, 11757 Cairo, Egypt.*

[4]*Research Unit, Physics of Insulating and Semi-insulating Materials, Faculty of Sciences, University of Sfax, B.P.1171, 3000 Sfax, Tunisia.*

[5]*Multidisciplinary Nanotechnology Centre, College of Engineering, Swansea University, Swansea SA1 8EN, United Kingdom.*

[6]*Center of Nanotechnology, King Abdulaziz University, Jeddah, 21589, Saudi Arabia.*

[7]*Research Center for Advanced Materials Science (RCAMS), King Khalid University, Abha 61413, P.O. Box 9004, Saudi Arabia.*

ABSTRACT

In this proposed research, the samples of undoped and several concentrations of praseodymium-doped zinc oxide (Pr_2O_3- ZnO) nanoparticles ranged from 0.001 g to 5 g were synthesized using a combustion technique as a simple, efficient, inexpensive, and environmental method. The structure, morphology, and chemical bonding were investigated by X-ray diffraction (XRD), and scanning electron microscopy (SEM), respectively, of the prepared Pr_2O_3-ZnO photocatalysts. The attained data from the previous devices sustained the ZnO growth from crystalline to satisfactory nanoparticle structure through changing the Pr^{3+}-doping concentrations inside the host matrix. Furthermore, the optical features have been investigated via UV-Vis diffused reflectance spectroscopy (DR), and AC electrical conductivity was studied to investigate the Pr^{3+}-nanoparticles' influence on the optical characteristics, energy bandgaps, of all proposed Pr_2O_3-ZnO nanostructured samples. The addition of Pr^{3+} dopants decreases the energy bandgap slightly and confines the photogenerated electron-hole recombination. The studied Pr_2O_3-ZnO nano-samples have been applied in photocatalytic degradation of methylene blue (MB) as an example for organic dyes and p-chlorophenol (p-CP) under visible light irradiation. The influence of Pr^{3+}-concentration, H_2O_2

concentration, and pH of the medium on the photocatalytic reaction have been studied. As the praseodymium doping ratios increased; the photocatalytic efficiency increased. After the addition of moderate Pr^{3+}-doping, further generation of hydroxyl radicals over ZnO. For 1% Pr^{3+}-ZnO, the optimal photocatalyst is a degradation of 100% of p-chlorophenol and methylene blue solutions. The prepared Pr_2O_3-ZnO nanostructured samples are amazing, promising candidates in novel potential nano-applications for wide-ranged from varistors, wastewater treatments, biomedical and photocatalytic degradation for phenol and organic dyes to different environmental fields.

Keywords:

Nanocomposites, Pr_2O_3-ZnO nanostructures, combustion technique, optical energy bandgaps, electrical properties, diffused reflectance, photocatalytic.

Corresponding author:** ***T.H. AlAbdulaal*

Tel.: +966-54080-6213

Email Address: talabdulaal@kku.edu.sa

1. Introduction

In recent years, scientific study has given more attention to developing human society, especially in wastewater treatment [1]. Dyes, pesticides, and weighty metals in water possibly will be the source of environmental pollution. Among those contaminations, organic dyes are considered one of the numerous novel chemicals, extensively applied in various fields, including leather, pulp, fabric, paper, medicinal, and cosmetic applications [2]. These organic dyes negatively affect the living things' health on Earth due to their cancer-causing and toxins [3]. Chemically, these persistent pollutants are carbon-based materials, which are naturally difficult to degrade and could not be practically removed by the traditional methods, including physical, biological, and chemical procedures. It could be highly effective costly to implement the exclusive chemicals as well as electrical energy consumption to eliminate the pollutants because of the stability of oxidants, which requires massive resources of energy and generates dangerous subordinate wastes, like weighty metals, deadly sludge, and solid waste [4]. Phenolics compounds are distinctive wastes because of their use by producing different engineering products, including plastics, textiles, gunpowder, pesticides, and dyes, [1], where most of these products have savior toxic effects on many living fields [5]. It is difficult to depend on the traditional techniques of organic treatment to remove phenols due to their strong stability and toxicity.

Taking advantage of wide-ranging applications and extensive productions, organic dyes have also been well-thought-out as a fundamental element of industrial wastewaters, commonly resistant and toxic for degradation through biological treatment techniques. Thus, traditional treatment techniques are unsuccessful for either mineralization or degradation of organic dyes [6]. Lately, ultrasound applications have gained extreme attention for wastewater treatments because of their operation easiness and large efficiency. Ultrasound has been utilized to handle different contaminants, like organic dyes, aromatic, and organic sulfuric compounds [7]. Nevertheless, organic compounds' degradation via ultrasound method consumes huge quantities of energy; add to that, complete mineralization of organic contaminants hardly occurs via sonolysis [7].

Organic dyes and phenolic derivatives are essential ingredients in industrial wastewater. They are produced on a large-scale due to their extensive applications because developing countries' backbone is industries. The organic by-products contaminants emitted by the factories such as coal tar, synthetic resins, pesticides, pharmaceutical tanning, textile, pulp mills, paint stripping, petroleum refining operations, and agricultural chemicals cause water pollution

[1]. These compounds are harmful because they are very stable and can persist for a long time in the atmosphere, whereas the biodegradation of phenolic contaminants is very slow. Methylene blue (MB), which has a heterocyclic aromatic structure and is environmentally toxic, especially to aquatic organisms, is the most common dye used for cotton, silk, and wood in the industry [2]. Furthermore, chlorophenols, a toxic substance commonly used in the plastics industry in the manufacture of polycarbonates and epoxy resins, have enabled the scientific community to research their effects due to their widespread release into industrial wastewater [3]. They were toxic and, by biological treatment methods, it is resistant to degradation. Therefore, traditional treatment methods are ineffective for organic dye degradation and mineralization [4].

To overcome those restrictions, an ultrasonic method could be utilized for wastewater treatments with an appropriate catalyst. Semiconducting nanomaterials are considered as so effective nanocatalysts, rendering to the literature [8]. The investigation for novel energy has attracted intensive focus to face exhaustion of energy sources and environmental pollutions. Semiconductors with multi-phase were verified as promising candidates through technological energy applications, photocatalytic removal of toxic chemicals in water and electrocatalytic, and photocatalytic creation hydrogen from water [9]. Among the plentiful semiconductors that are used in the photocatalysis field such as TiO_2, ZnS, ZnO, and Fe_2O_4, ZnO nanoparticles is one of the greatest typical nanomaterials taking advantages of its inexpensive cost, natural chemical stability, and non-toxic behaviors [10]. ZnO nanoparticles are extensively applied in luminescence, sensors, solar cells, catalysts, biomedical and optoelectronics devices, and light-emitting diodes [11]. Zinc oxide (ZnO) nanoparticles have an extensive focus in nanoscience research due to the distinctive direct large bandgap of 3.37 eV as well as the exciton binding energy of 60 meV [12]. Additionally, ZnO studies have been gained concentrated efforts; taking advantage of its remarkable properties, such as large electrochemical coupling index, high chemical stability, adequate thermal conductivity, small dielectric constant, antibacterial, binding, and UV-protection and as well as large refractive index and transmittance in the visible to infrared ranges. As a result, the unique ZnO's optoelectronic characteristics open the windows to be applied in widespread technological applications including, gas sensors, piezoelectric transducers optical waveguides, varistors, blue and ultraviolet (UV) optical devices, UV- light emitters, transparent conductive films, thin-film transistors, solar cell windows, biological, biomedical and chemical gas sensors, and bulk acoustic wave and optoelectronic devices [11].

Amongst various photocatalysts, ZnO was broadly utilized in the photocatalytic procedures to eliminate the organic dyes in wastewater treatments due to its low cost and large bandgap [12]. The central challenge of undoped ZnO nanoparticles is the rapid recombination rate of the formed electron-hole pairs [13]. Therefore, to expand photocatalysts' efficiency, the recombination of the electron-hole pairs must be fundamentally impeded. ZnO nanoparticles could be improved by doping metal ions to boost structural, optical, and chemical properties, promising to decrease the possible recombination rate of the formed electron-hole pairs as potential candidates [12]. For example, sulfur-doping could enhance the lattice constants of the ZnO semiconductor and increase the oxygen vacancy [13].

On the other hand, the photocatalytic properties of ZnO nanomaterials could be enhanced using different preparing approaches, like solid-state reaction, sol-gel, and solvothermal [14]. Recently, it has been revealed the enhancements of photocatalytic activity via doping with non-metal and metal, as well as the spectral response, were enhanced with better sunlight usage. Thus, altered photocatalysis of semiconductor oxides demonstrates great technological candidates for treating environmental pollutions, which have been developed to be a moderately popular research study in the previous few years [14].

One of the effective techniques to get rid of such contaminants is semiconductor photocatalysis. Oxides, such as TiO_2, ZnS, CdS, SnO_2, Fe_2O_3, Cu_2O, and ZnO, are commercially usable photocatalysts. In the photodegradation of organic compounds under sunlight and solar-simulated radiation, ZnO is more commonly used. Susceptibility and UV-tail absorption are high [15]. Based on these benefits, organic water contaminants are completely photodegraded into non-hazardous minerals by ZnO nanoparticles as photocatalysts. The challenge of narrowing its bandgap and improving its optical and photocatalytic activity provides these characteristics. Consequently, doping ZnO with praseodymium (Pr) would boost its properties and, ultimately, its applications. Rare-earth doped nanomaterials have stimulated wide interest and are practically used in several optoelectronics devices like optical light-emitting phosphors [15].

There was no information about the Methylene blue (MB) and p-chlorophenol (P-CP) photodegradation in aqueous solution by the Pr^{3+}- ZnO to the best of the recent information photocatalyst using the irradiation of simulated solar light. Several research studies investigate praseodymium (Pr) rare earth elements to augment ZnO's photocatalytic and optical properties [16]. However, there haven't plentiful studies that emphasize Pr^{3+}- ZnO nanocomposites to be used as photocatalysts, varistors ceramic and biosensors, and optoelectrical devices. Therefore, the current research intends to investigate the Pr^{3+}-dopant effects on the morphology, structure,

optical, and electrical properties of the host ZnO nanoparticles as well as to study the dependency between the photocatalytic behavior and the concentration ratio of Pr^{3+}-dopant, which are verified through degradation of Rhodamine-B (RhB) dye in water under visible illumination. As a result, all prepared Pr_2O_3-ZnO nanostructured samples, smart and multifunctional, are promising candidates for wide-ranged environmental, technological, and electronic and dielectric applications, like varistors and photocatalysis, and biosensors.

2. Experimental techniques

2.1. Materials Synthesis

In this current study, samples of both undoped ZnO nanoparticles (NPs) and doped with praseodymium (Pr^{3+}) were manufactured using a combustion method. Firstly, in ceramic crucibles, five grams of $Zn(NO_3)_2.6H_2O$ was blended and completely crushed. Then one gram of gum acacia was added, with individually eight various concentrations of praseodymium (Pr) ranged from 0.001 g to 5 g, that was called So to S7, respectively in Table.1, to the earlier mixture, where the mixture dissolute in 5 mL of distilled water. The synthesis combinations of Pr_2O_3 -ZnO nanocomposite were heated at 600 ^oC for two hours and then cooled down at ambient temperature. In this preparation method, gum acacia was utilized as a fuel for assisting the change of the ZnO structure from crystallinity to nanoscale through increasing the constituents inside the matrix.

Table. 1. The sample code of ZnO-nanostructures with different doping concentrations of Praseodymium Pr^{3+}-ions.

Samples	Codes
Pure ZnO	So
0.001g Pr-doped ZnO	S1
0.01 g Pr doped ZnO	S2
0.1 g Pr doped ZnO	S3
0.5 g Pr doped ZnO	S4
1 g pr doped ZnO	S5
2.5 g Pr doped ZnO	S6
5 g Pr doped ZnO	S7

2.2 Devices & Measurements.

X-ray diffractometer (XRD) is a powerful technique utilized in studying the structure of the synthesis of Pr_2O_3- ZnO nanostructured samples. In this current report, XRD analysis was examined via Shimadzu LabX-XRD-6000 utilizing filtered radiation of CuK_α (λ = 1.5406 Å) at ambient temperature. The scanning electron microscopy (SEM), which is JSM-6360 type

with an operating voltage of 20 kV, was utilized to examine the morphology of the surface of all prepared Pr_2O_3–ZnO nanocomposites in power form.

Additionally, the UV-Vis spectrum of all prepared Pr_2O_3–ZnO nanostructured samples were analyzed over an integrated sphere device coupled to a 3600 UV-Vis spectrophotometer (Shimadzu, Japan). At this point, the wavelength ranged from 200 nm to 1600 nm with a 5 nm step scan, where the calibrated standard sample is barium sulfate.

At a constant temperature of 25 ^oC, the electrical measurements of the synthesized Pr_2O_3–ZnO nanocomposites were accomplished utilizing a computerized digital Keithley 4200-SCS with a wide range of frequency from 3 kHz to 10 MHz. At room temperatures, the current-voltage was measured using the typical circuit controllable PID. The circuit involves a digital pico-ammeter, that has the model of DPM-111/SVS labs Inc. USA, power supply with high-voltage from the model EHT-11/SVS labs Inc. USA, as well as PID controlled oven with the model of PID–200 that is linked to double probe holder, which is fixed in a distinct oven that is attached to the operating system.

2.3 Photocatalytic Measurements

Methylene blue and p-chlorophenol as different types of organic pollutants have been applied for photocatalytic experiments in the presence of all the as-prepared photocatalysts samples to investigate their photocatalytic efficiency in a thermo-stated photoreactor equipped with a multi-position magnetic stirrer under various experimental conditions. 0.01 g of each sample from each set of the investigated nano-powders has been added to 100 ml of organic compounds solution, either MB or p-CP, separately. The system could work in the dark for about 30 minutes until the equilibrium condition was reached to study chemisorption. After an interval time of irradiation of about 10 minutes, 5 ml of the solution sample was extracted and centrifugated at 3000 rpm to remove all powder suspension. The rest of the mixture has been subjected again to visible light. Every 15 minutes of irradiation, sample activity was evaluated. Finally, the photo-degradation process was detected in the wavelength range from 200 to 800 nm, using the JASCO V-550, Japan, the UV-Vis spectrophotometer analyzes samples through the absorbance versus wavelength measurements.

3. Results and discussions

3.1 Morphological characterization

3.1.1 X-ray Diffraction Pattern (XRD) of nanostructured Pr_2O_3–ZnO.

From Fig. 1, it is noticeable that the Pr_2O_3–ZnO phase does not take place in a low doping ratio, and that phase appears to be increased with increasing the Pr-doping concentration. The dislocations in a crystal are an imperfection related to the lattice's misregister in one part of the crystal concerning another part. The XRD patterns of pure ZnO matrix and Pr_2O_3-ZnO nanostructured present mostly diffraction peaks that agree with the standard data due to the wurtzite ZnO phase (JSPDS 01- 075-0576) with weak lines related to carbon phase (JSPDS 01-074-2328) [17]. Amazing features can be seen in the XRD spectra of the P_2O_3–ZnO phase (JSPDS 01- 083-1193). The significant peaks were corresponding to (101) and (100) planes have been noticed in all investigated nano-samples, which perfectly agreed with the published XRD results of ZnO by K.-S. Yu et.al. They proved the main XRD peaks that site at 31.8°, 34.4°, 36.3°, 47.5°, 56.6°, 62.9°, 66.4° angles, consistent with the indexed of (100), (002), (101), (102), (110), (103), and (201). The wurtzite structure of the prepared pure ZnO sample was indicated by those prominent XRD peaks [17].

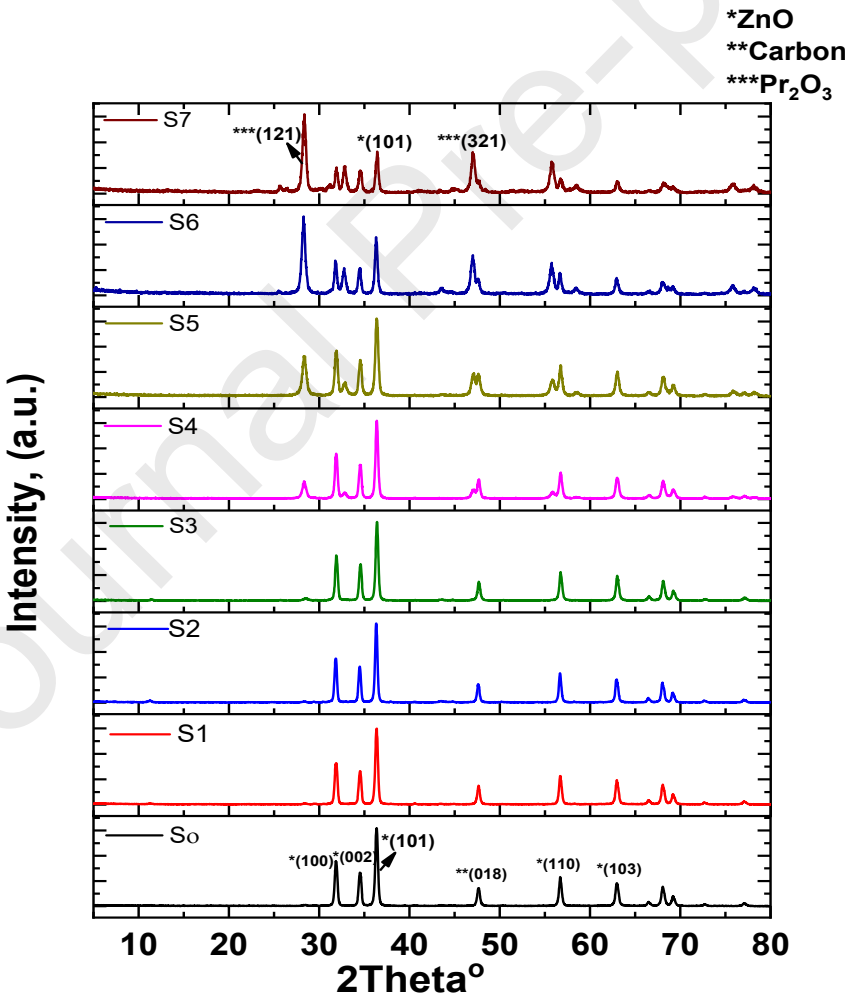

Fig. 1. XRD patterns of pure ZnO and Pr_2O_3–ZnO nanostructured samples, with different praseodymium doping concentrations.

A small shift in *2θ* value towards the left for the (002) plane has certainly been examined for the undoped ZnO material. XRD analysis confirms that praseodymium doping content noticeably influences the structure of crystallinity of the combustion synthesis Pr_2O_3-ZnO powder and has significant effects on the formation of the Pr_2O_3 phase, which was started to be appeared with increasing praseodymium concentrations. L. Zhang et. al stated that co-doping of Pr and N would improve the ZnO efficiency for solar cell applications [18]. XRD technique was used to investigate the structure morphology and chemical composition of the prepared Pr: N: ZnO samples, which had a structure of hexagonal wurtzite. The obtained XRD results successfully proved the incorporation of Pr and N atoms in the ZnO lattice [18].

From XRD and SEM analyzed data, the computed grain size in nanometres, the density of dislocation (η) in $(nm)^2$, and the lattice strain (ε) for all phases of the as-prepared host ZnO with differing praseodymium doping concentrations (Pr_2O_3–ZnO) were defined.

At this time, the flowing of Scherrer's equation was applied to investigate the XRD data, which was used to calculate the crystallinity size (D) of the synthesized Pr_2O_3–ZnO nanocomposite materials through the following equation [19]:

$$D = 0.9\lambda/\beta\cos\theta, \quad \textbf{(1)}$$

Moreover, the average values of the crystallite size of all as-prepared Pr_2O_3–ZnO nanostructured were determined from 13 to 40 nm, where they typically agree with a particle size that was evaluated from XRD analysis. J. Wang et.al studied TiO_2 - doped ZnO composites and the particle size on average was around 80 nm, according to Scherrer's formula [30]. Additionally, the calculated grain size of Pr: ZnO nanocomposites were in the range between 17 and 23 nm in good match with the reported values of the average grain size (15-19 nm) for Nd and Pr: ZnO, which were prepared and characterized by D.Venkatesan et.al [16].

3.1.2. Scanning electron microscopy (SEM) analysis of nanostructured Pr_2O_3–ZnO.

In this proposed work, scanning electron micrographs (SEM) were applied to investigate the synthesized Pr_2O_3-doped ZnO nano samples' growth topographies. Fig. 2 illustrates SEM images to examine the structure morphologies of the analyzed Pr_2O_3–ZnO nanostructured at different praseodymium doping concentrations ranging from 0.001 g to 5 g. The differences in the pure ZnO matrix's structure morphology and praseodymium doped ZnO nanocomposites were noticeable. The SEM images of the Pr_2O_3–ZnO nanostructured samples generally showed a uniform distribution of Pr-ZnO spherical nanoparticles. Generally, the praseodymium ions create small-sized grains and promote the crystal nucleation rate, while the

trapping of praseodymium grains stops the grain development. This issue may be due to the variation in ionic radius between zinc and praseodymium [11].

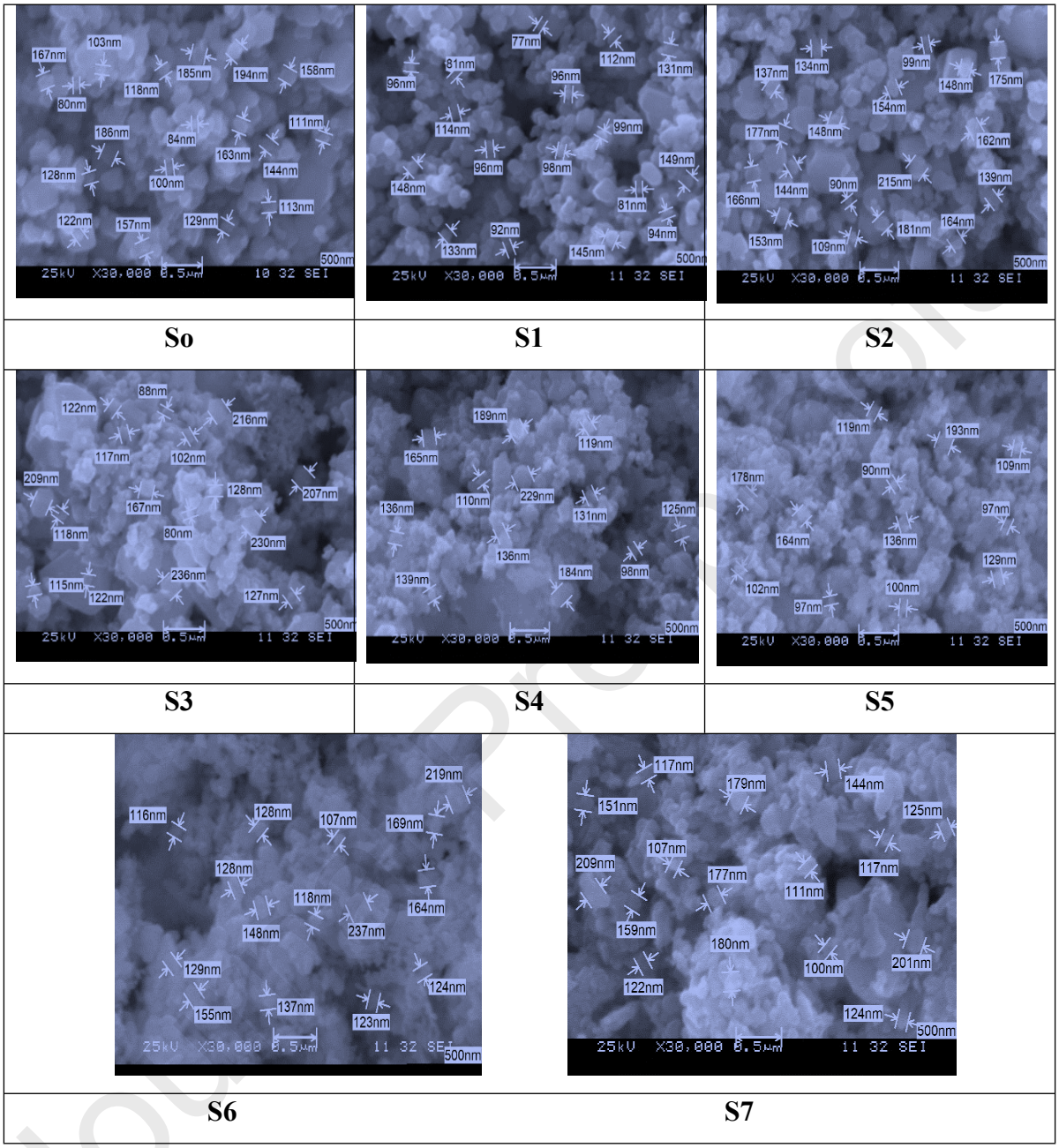

Fig. 2. SEM images of pure ZnO and Pr_2O_3–ZnO nanostructured samples, with different praseodymium doping concentrations.

With the increase in the praseodymium doping ratio, the shape and the size of the nanoparticles changed. As a result, the achieved SEM findings agreed very well with the XRD analysis. SEM images of undoped ZnO nanoparticles and Pr-doped ZnO nanostructures displayed the mean grain sizes calculated from morphology analysis are about 135 nm for host ZnO nanoparticles and around 145 nm Pr-doped ZnO nanocomposites, which were in great

agreements with the XRD data. Both the size and the shape of the Pr nanoparticles changed with increasing the dopant concentrations in ZnO. The obtained SEM results in this current study matched with the SEM conclusion of the ZnO morphology that was investigated by P. Banerjee et. al [20]. The grain size of those particles was 200 nm on average, which was calculated from SEM images [20]. The SEM results showed that as the praseodymium ratio increased, the crystalline size reduced.

3.2. Optical properties of nanostructured Pr_2O_3–ZnO.

3.2.1. Optical Diffused reflectance (ODR), absorption index, and bandgap analysis of nanostructured Pr_2O_3–ZnO.

The diffuse reflectance (ODR) measurement is considered a conventional technique applied to collect optical data for the studied Pr_2O_3–ZnO nanopowders. Separately, Fig. 3 (a,b) describe the optical diffused reflectance (ODR) and the absorption index (k) of the Pr_2O_3–ZnO nanostructured materials as a function of light wavelength in the range of 200 nm to 700 nm. From Fig. 3(a), it is noticeable that there are no many differences between the diffuse reflectance (ODR) of all prepared samples understudy in the wavelength range of 200 nm to 370 nm. After that, the ODR spectra detected a sharp increase within the wavelength ranges from 370 nm to 410 nm, creating the optical bandgap edge. The ODR spectra showed almost increased lines within the wavelength ranges from 410 nm to 700 nm for the studied materials. In the end, the absorbed light via the deliberate Pr_2O_3–ZnO nanocomposites produces the optical absorption bandgaps [21].

Moreover, Fig. 3(b) showed that the investigated Pr_2O_3–ZnO nanostructured samples have low absorption index values (k), between $1x10^{-4}$ and $1x10^{-3}$, due to the non-absorbent surface area of the Pr_2O_3–ZnO nano-compounds as predisposed to the incident light. Also, this figure showed the maximum absorption values at a light wavelength = 380 nm, characteristic for the electronic transitions from band to band ($\pi \rightarrow \pi^*$) [22]. In this present study, the obtained ODR results are matched with the published work by A.R. Khataee et. al, where they prepared and optically study ZnO nanoparticles doped with different concentrations of dysprosium [29]. At the visible region, the Dy-doped ZnO composites illustrated a strong absorption with redshift, as seen in DRS spectra [11].

The following equations of Tauc's model were applied to calculate the optical bandgaps E_g of the synthesized Pr_2O_3–ZnO nano-powder as [23].

$$(\alpha h\nu)^{1/n} = A^{1/n}(h\nu - E_g), \quad \textbf{(2)}$$

In Eq. (2), α is identified as the absorption index, t is the thickness of the material (i.e. thickness of the holder), and as well as, $h\upsilon$ is recognized as the photon energy of the electromagnetic (EM) radiation, υ is known as the photon frequency, h is Planck constant, A is the band tailing factor and its values are in the range of (1×10^5 - 1×10^6 $cm^{-1}.eV^{-1}$) [24], and E_g is the optical energy bandgap of the studied material. Additionally, in the earlier Eq. (2), the n = ½ for direct bandgaps or n = 2 for the indirect bandgaps. The relation of $(\alpha h\upsilon)^{1/2}$ and $(\alpha h\upsilon)^2$ as a function of the photon energy ($h\upsilon$) for as-prepared Pr_2O_3–ZnO nanocomposite samples at several praseodymium concentrations are separately illustrated in Fig. 3 (c,d).

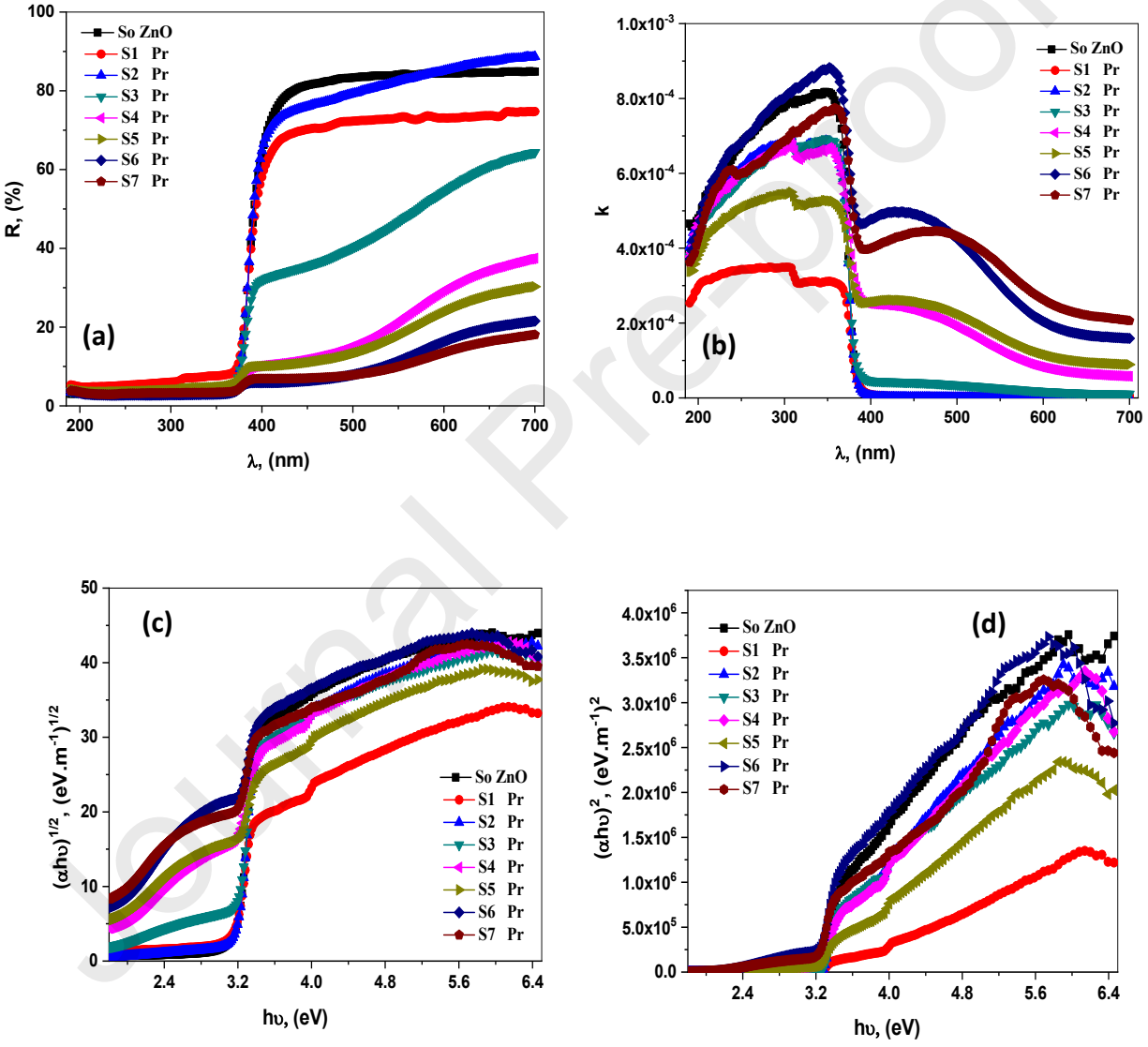

Fig. 3. (a) Optical diffused reflectance (ODR), (b) Absorption coefficient (k), (c) optical allowed direct transition $(\alpha h\upsilon)^{1/2}$, (d) the optical allowed indirect transition $(\alpha h\upsilon)^2$ of pure ZnO and Pr_2O_3–ZnO nanostructured samples, with different doping concentrations.

The direct and indirect optical bandgaps have been found through the intercept line for the studied curves at the intercept where $x = 0$, as shown in Table. 2, where $\alpha^{1/2}$ and α^2 reached zero. The direct bandgap's values for the Pr_2O_3–ZnO nanostructures Pr_2O_3–ZnO differ between 2.34 eV and 3.06 eV. While the determined values for the indirect allowed optical transition were in the range from 3.01 eV to 3.587 eV. These values were established to be lower than those values for the host ZnO nanoparticles. The bandgap values decrease with increasing the concentration ratio of Pr_2O_3 dopants due to the creation of novel energy states among the valence and the conduction states. The calculated bandgaps of Pr-doped ZnO nanocomposites are in good agreement with the reported optical results for sol-gel prepared samples of ZnO nanoparticles doped with Fe by C. Aydın et. al [25]. The optical bandgap value of undoped ZnO was calculated to be approximately 3.19 eV, which decreases to around 2.75 eV with rising concentration ratios of Fe dopant [25].

Table. 2. The calculated optical bandgaps for both direct and indirect transitions of Pr_2O_3 - doped ZnO nanoparticles.

Samples	***E_{g1}(d), eV***	***E_{g1}(ind), eV***
So	3.066	3.236
S1	3.026	3.587
S2	3.054	3.326
S3	2.944	3.248
S4	2.642	3.18
S5	2.584	3.11
S6	2.43	3.01
S7	2.34	3.02

3.2.2. Dielectric behavior & AC electrical conductivity of nanostructured Pr_2O_3–ZnO.

The dielectric function $\varepsilon^*(\omega)$ simplifies the direct reaction of the material to the electromagnetic radiation (EM) and $\varepsilon^*(\omega)$ also controls the propagation performance of EM waves in the investigated media. Therefore, it is very significant to describe the origin and nature of the dielectric function. For Pr_2O_3–ZnO nano-powder, the following equations could be used to determine the complex dielectric function $\varepsilon^*(\omega)$ [26]:

$$\varepsilon^*(\omega) = \varepsilon_1(\omega) + i\varepsilon_2(\omega), \quad \textbf{(3)}$$

Where

$$\varepsilon_1(\omega) = \frac{C \times l}{\varepsilon_0 \times A}, \quad \text{and} \quad \varepsilon_2(\omega) = \tan\delta \times \varepsilon', \tag{4}$$

The part of the dielectric constant here is $\varepsilon_1(\omega)$, whereas $\varepsilon_2(\omega)$ is the imaginary component. Furthermore, ε_o is the permittivity of free space, A is the area of the electrode, *tan* δ is the loss tangent, and C, l, and Z are the capacitance, thickness, and impedance of the sample, respectively. From Fig. 4 (a), as displayed in the low-frequency regions, the dielectric constants decline significantly as the photon frequency increases up to 16. Then, the dielectric constants decrease a little with the rise of the incident frequency. Enhancing the dielectric constants with a frequency reduction discloses that the Pr_2O_3–ZnO nanocomposites determine large interfacial polarization in the low-frequency regions. At the higher frequency values, the dielectric constant values increase and reach the maximum value of about 31. Furthermore, the reduction in the dielectric constant values is faster in the Pr_2O_3–ZnO nanocomposites with a higher doping concentration of praseodymium contents. The obtained dielectric values of Pr-doped ZnO nanocomposites in this current study agreed very well with the published results by [20]. The dielectric constant of ZnO nanoparticles ranged in values between 19.92 and 32.6 [20].

Moreover, the dielectric loss values reduce to the lowest possible point and then enlarge once more, as shown in Fig. 4 (b). The reduction of the dielectric constants of the considered Pr_2O_3–ZnO nanomaterials is commonly affected by the dielectric polarization mechanism. To underline, some kinds of dielectric polarization may be found as ionic, interfacial electronic, or dipolar polarization when an external field is applied to the Pr_2O_3-ZnO nanoparticles. It can be concluded that ionic and electronic polarizations are controlled in the high ranges of the incident frequency. In the lower frequency region, the maximum value of the dielectric loss $\varepsilon_2(\omega)$ could be realized through the interfacial polarization mechanism due to charge carriers, which determine and limited by defects and grouped in the dielectric medium. When the frequency becomes higher, the $\varepsilon_2(\omega)$ starts to increase because of the dipole oscillation, which can quickly rotate [27]. The difference of both dielectric constant $\varepsilon_1(\omega)$ and dielectric loss $\varepsilon_2(\omega)$ versus the frequency is ranging from $3x10^3$ Hz to 10^7 Hz as displayed in Fig. 4 (a,b). The dielectric constant values are large in comparison to the dielectric loss values, where both of them are dependent on k and n values. To prove, the dielectric constant and loss values were high at low-frequency ranges but were trivial in the long region, where those obtained dielectric results mostly agreed with the published data by P. Maji et. al [28]. They

observed that the dielectric constant of Zn $(NO3)_2$ particles decline as a function of the polarization. Generally, the reduction of the dielectric constants of the considered materials' is associated with the dielectric polarization's mechanics.

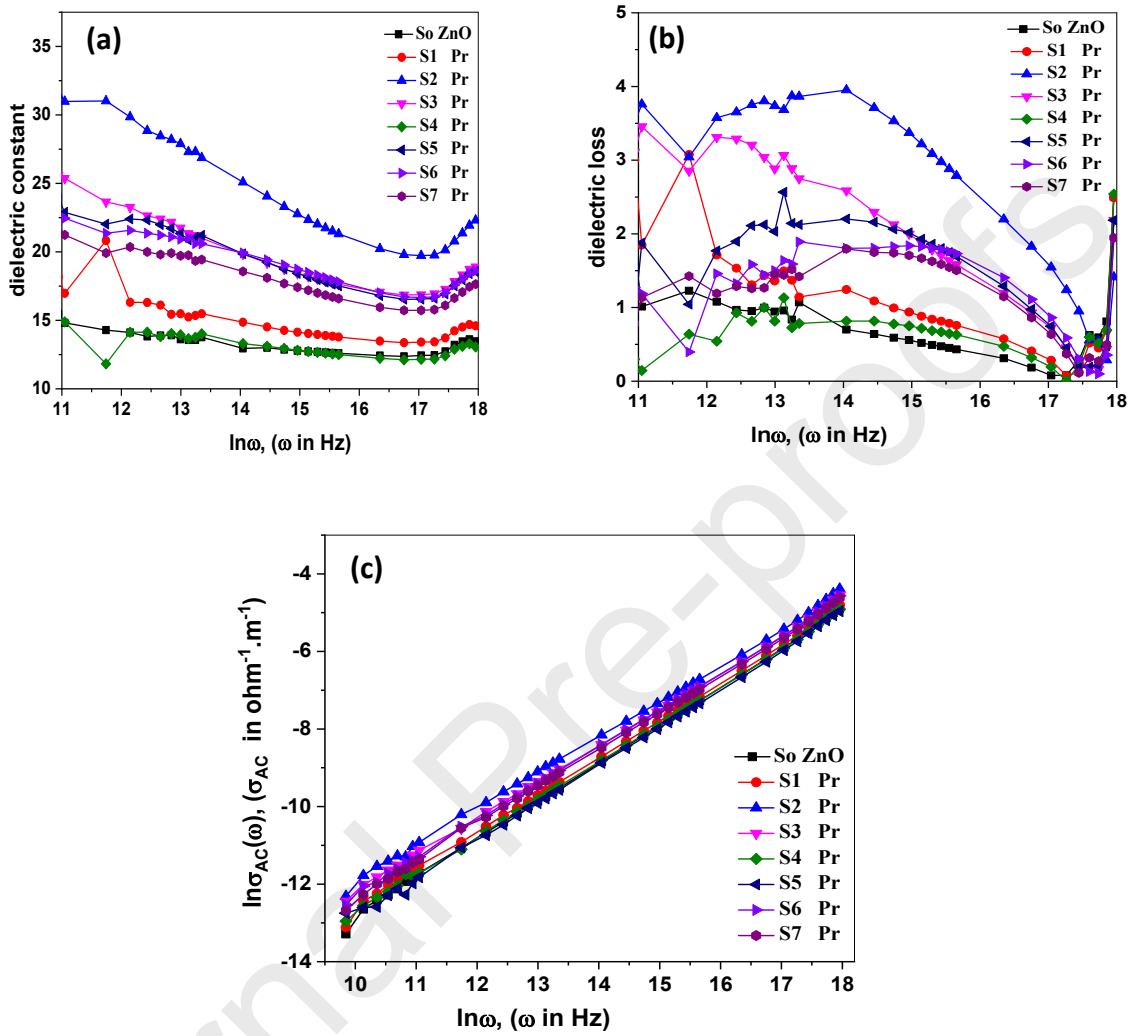

Fig. 4. (a,b). Presenting the dielectric constant and loss, (c) the AC electrical conductivity as a function of the frequency of pure ZnO and Pr_2O_3–ZnO nanostructures, with different Pr doping concentrations.

It is important to consider that the photon frequency affects AC electrical conductivity to discuss the conduction mechanism of the Pr_2O_3-ZnO nanostructured materials at various doping ratios of praseodymium. To calculate the AC conductivity of the studding materials, the following equations can be considered [29]:

$$\sigma_{Total.AC}(\omega)=\frac{t}{ZA}, \quad \textbf{(5)}$$

$$\sigma_{Total.AC}(\omega)=\sigma_{DC}(\omega\to 0)+\sigma_{AC}(\omega), \quad \textbf{(6)}$$

$$\sigma_{AC}(\omega) = A\omega^{S}, \quad (7)$$

At this point, the total AC electrical conductivity is recognized as $\sigma_{Total.AC}(\omega)$, the impedance is known as *Z*, and *A* is a constant depends on the temperature, which shows the diffusion of conductivity and dielectric behavior of the filling medium. Also, respectively, $\sigma_{DC}(\omega \to 0)$ and $\sigma_{AC}(\omega)$ are known as the DC and AC electrical conductivities, where the angular frequency is ω, and the frequency exponent is donated as *s*. The obtained values of AC electrical conductivity is in the range between 10×10^{-9} and 10×10^{3} $\Omega^{-1}.cm^{-1}$ [30]. Eq. 7 indicates that the AC electrical conductivity plays an important role in many-body interaction, which describes the power-laws universal behavior. The frequency exponent (*s*) is a vital parameter that showed the multi-interaction between the material impurities and the charge carriers. Here, the *s* value depends on the incident frequency and temperature, where its value differs from zero to one. It is equal to one for standard Debye type media. The *s* frequency parameter is correlated to either charge carriers or inessential electrical dipoles caused by impurities. The values of the frequency exponent range between 0.6 to 0.8, and it was around one for highly disordered dielectric mediums [30].

The computed values of $ln\sigma_{AC(\omega)}$ was presented in Fig. 4 (c) versus ln(ω) for all prepared Pr_2O_3- ZnO nanoparticles. The AC electrical conductivity values rise linearly with the photon frequency, including increasing the Praseodymium concentration on the manufactured Pr_2O_3-ZnO nanostructures. At room temperature, the frequency exponent (*s*) values were determined from the slope of the obtained linear cures in the earlier relation. In this current study, S's estimated values were almost around one (0.98) [29].

3.3. Current-Voltage characteristics of nanostructured Pr_2O_3–ZnO.

The *V-I* characteristics exhibited of the studied samples-based varistor ceramics consist predominantly of pre-breakdown, breakdown, and upturn regions. The varistor action takes place in the breakdown region. In this region, the applied voltage is a highly nonlinear function of the current and can be described by the empirical law [31]:

$$I = KV^{\alpha} \quad (8)$$

where *V* is the applied voltage, *I* is current, *K* is a constant depending on the geometry and manufacturing process and α is the nonlinear coefficient. The value of nonlinear coefficient α is obtained from the inverse of the slope of the *lnV* - *lnI* curves at any voltage value.

Fig. 5 (a–h) illustrated the relations between voltage (V) and the current (I) of the Pr_2O_3–ZnO based ceramic varistors. From these figures, all samples showed obvious nonlinear behavior. As result was reported by D. Xu et. al, all specimens display a highly nonohmic behavior [32].

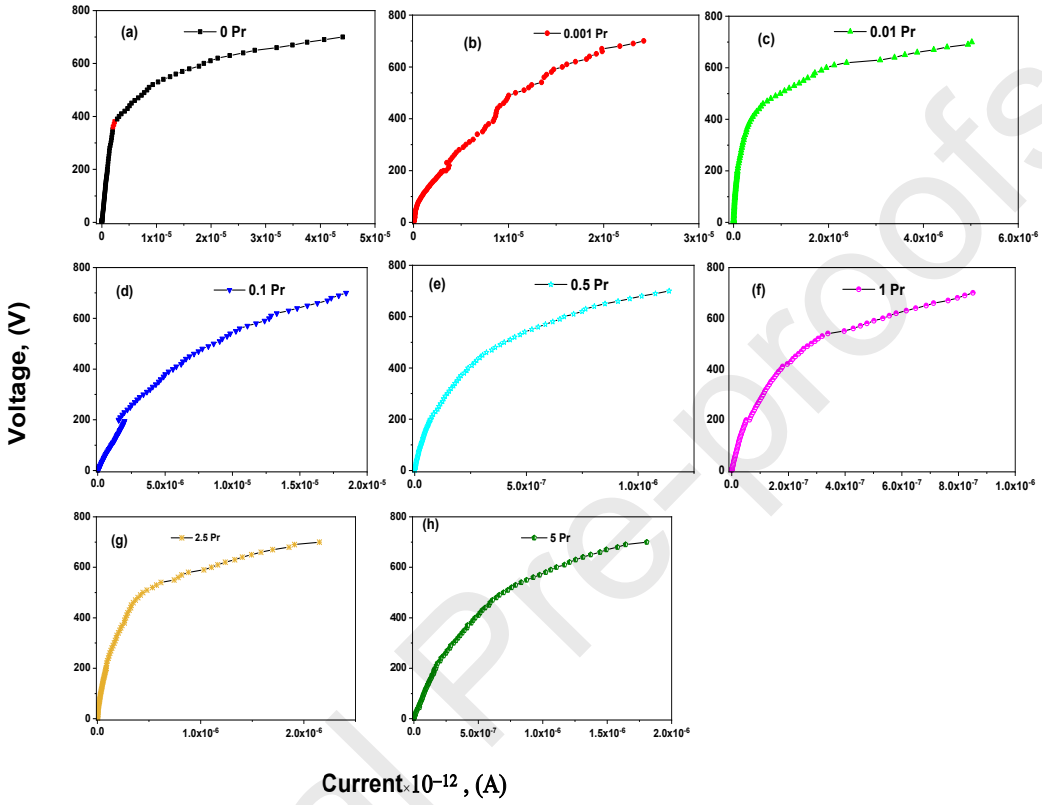

Fig. 5. The *V-I* characteristics of pure ZnO and Pr_2O_3-ZnO nanostructured, with different praseodymium doping concentrations for ceramic varistors.

The curves showed the conduction characteristics are divided into two zones: a high impedance linear region below the knee-point voltage and a low impedance non-linear region above the knee point voltage. C.W. Nahm found that the knee-sharper of the plots between the two regions is characterized by the better nonlinear property [33].

The detailed nonlinear characteristics can reveal the nonlinear coefficient a, threshold voltage V_{ss} and leakage current I_R of the undoped and Pr_2O_3–ZnO ceramic varistors. The AC impedance parameters have been analyzed the complex impedance ($Z^* = Z' + i\,Z''$) using the following functions below [34]:

$$Z' = \frac{1}{\omega c_o}\left[\frac{\varepsilon''}{\varepsilon'^2 + \varepsilon''^2}\right]; Z'' = \frac{1}{\omega c_o}\left[\frac{\varepsilon'}{\varepsilon'^2 + \varepsilon''^2}\right], \quad \textbf{(9)}$$

where ω is the chosen angular frequency, (ε', $\varepsilon''= \varepsilon' tan\delta$) are the real and imaginary portions of the dielectric permittivity and c_o is the vacuum capacitance. The real and the imaginary components of studied impedance were calculated as follows [34]:

$$Z' = \frac{R_{gb}^2 Q\omega^c \cos\left(\frac{c\pi}{2}\right) + R_{gb}}{\left(1 + R_{gb}Q\omega^c cos\left(\frac{c\pi}{2}\right)\right)^2 + \left(R_{gb}Q\omega^c sin\left(\frac{c\pi}{2}\right)\right)^2}, \quad \textbf{(10)}$$

$$-Z'' = \frac{R_{gb}^2 Q\omega^c \sin\left(\frac{c\pi}{2}\right)}{\left(1 + R_{gb}Q\omega^c cos\left(\frac{c\pi}{2}\right)\right)^2 + \left(R_{gb}Q\omega^c sin\left(\frac{c\pi}{2}\right)\right)^2}, \quad \textbf{(11)}$$

The average square-method used for simulating the resistance R_b, the CPE value indicated by Q, and the parameter c through the difference between experimental and theoretical results. The impedance of CPE is $Z_{CPE} = 1/A_o(i\omega)^c$. The grain boundary resistance R_{gb} was calculated from the Cole-Cole plot of impedance measurements. Fig. 13(a&b) presents the real and imaginary of the AC impedance properties versus the angular frequency of the undoped and Pr-doped ZnO specimens at room temperature.

Fig. 6 (a) reveals the Pr-doping has a great influence on the real part of the AC impedance properties of ZnO-based ceramic varistors. The simulation gives a good matching with the experimental data of the real part of the AC impedance. The observed value of real impedance is high at a lower frequency and gradually decreases with an increase in angular frequency which is related to the increase in AC conductivity and remains constant at the higher frequencies. This is associated with the polarization of dielectric characteristics. From Fig. 6 (b), the imaginary part of the AC impedance reveals that the Pr-doping ZnO-based ceramic varistors have not great effects with increasing the Pr compositions.

The experimental data of Fig. 6 (b) matches closely the theoretical of Eq. (17). At the higher frequencies, the experimental data of the imaginary part of AC impedance becomes constant. To determine the dielectric parameters from the AC impedance measurements of the undoped and Pr-doped ZnO-based ceramic varistors with various Pr-contents, Fig. 6 (c) illustrates the Cole-Cole diagram which necessary to investigate the equivalent circuit model of the studied nanomaterials. It is noticed that, from undoped to 0.1 g Pr-contents (S3), the ceramic varistor systems follow only portions of the arcs plots due to higher impedances at the lower frequencies. Meanwhile, up the specimen with 0.1 g Pr-content (S3), a linear behavior of the plots indicates that the specimens consist of a single resistor representing the ohmic contact resistance.

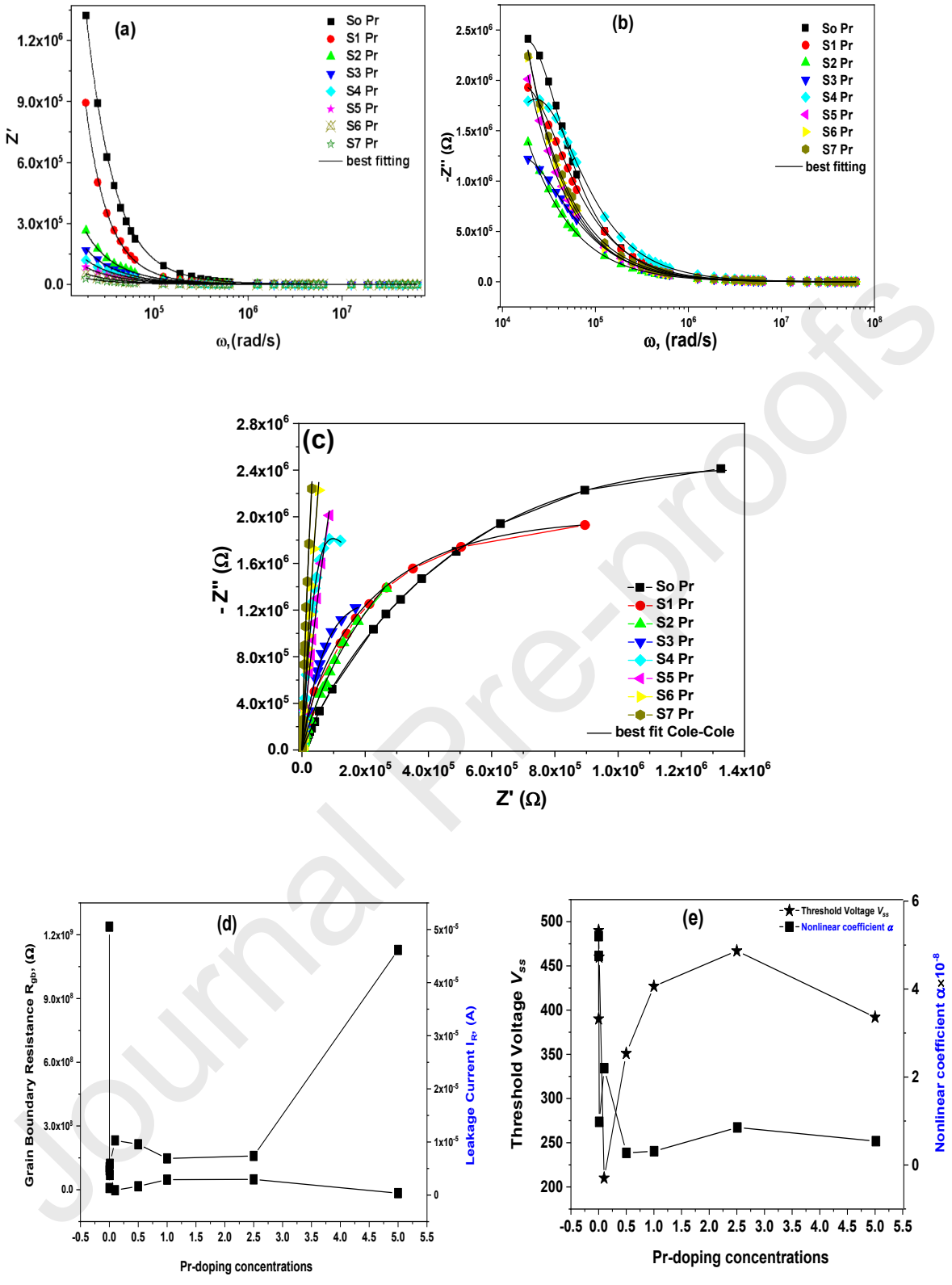

Fig. 6 (a-e). (a) Real, (b) imaginary parts, (c) Cole-Cole plots (the line represents the theoretical best Cole-Cole fitting), and (d,e) The *V–I* fitted parameters versus the Pr-contents of ZnO-based varistor ceramics of pure ZnO and Pr_2O_3-ZnO nanostructured samples with different praseodymium doping concentrations for ceramic varistors.

The arc begins to appear which indicating a capacitive contribution, which makes the ceramic varistor systems are a suitable candidate for capacitors devices. Based on the fitted experimental AC impedance data, the grain boundary resistance (R_{gb}) values of the studied systems were exposed as a function of Pr-contents, as shown in Fig. 6 (d). It is noticed that the decrease in leakage current with the increase of Pr-content is attributed to the increase in activation energy and the homogeneous distribution of Pr-content on the ZnO matrix for ceramic varistor material systems. In the previous work, Pr-doped ZnO–Bi_2O_3 varistors, or ZnO–Pr_6O_{11} varistors doped with Dy-ions and rare-earth-doped ZnO-based varistors materials [35]. It is necessary to ensure that the high level of effective barriers to the grain boundaries and increases its resistance and avoiding leakage currents in order to achieve higher values with a nonlinear coefficient. A graphical description relationship curves between the Pr-doping, the nonlinear coefficient α, and the threshold voltage V_{ss} of the ZnO-based ceramic varistors are schematically summarized in Fig. 6 (e). After an excessive increase of Pr-contents, the variation of the threshold voltage firstly decreased and then increased due to the decrease in the grain size of the ZnO-based varistor. Even a successive addition of Pr-amount positively influenced the nonlinear coefficient α. From Fig.6 (e), the nonlinear coefficients are raised as increasing the Pr- the amount in ZnO varistor systems.

3.4. Photocatalytic performance of nanostructured Pr_2O_3–ZnO.

The photocatalytic activity of studied samples has been evaluated through the photodegradation of MB and p-CP. The influence of Pr-doping in the ZnO matrix named as (Pr_2O_3-ZnO), pH, and [H_2O_2] on the photocatalytic activity were also studied in detail. All the photocatalytic experiments were taking place under visible light illumination. Before the light irradiation, all experiments were kept in the dark till equilibrium for studying the adsorption process. While the adsorption of MB and p-CP over Pr_2O_3-ZnO nanocomposites was neglected. It may be attributed to *pKa* values, which affect the interaction between the contaminates and the photocatalysts.

3.4.1. Kinetic study of the photocatalytic performance.

Figs. (7&7*) represented the photodegradation of MB and p-CP, respectively, using pure ZnO and Pr-doped ZnO NPs under visible illumination. The reactions follow Langmuir–Hinshel model. The kinetics and photocatalytic performance of the as-prepared NPs the % degradation of MB and P-CP can be calculated using [36].

$ln(C/C_o) = -kt$, **(12)**

$\%\ of\ degradation = (C_o\text{-}C/C_o) \times 100\ \%$, **(13)**

As C_o is the concentration at 0 min of irradiation, at time t, the concentration is C with constant rate k. The decrease in the concentration of MB with time was represented in Fig. 7 (a). The Kinetic data of photodegradation of MB in Fig. 7 (b) illustrated that the reaction rate constant ranged from 0.053 to 0.135 min^{-1}.

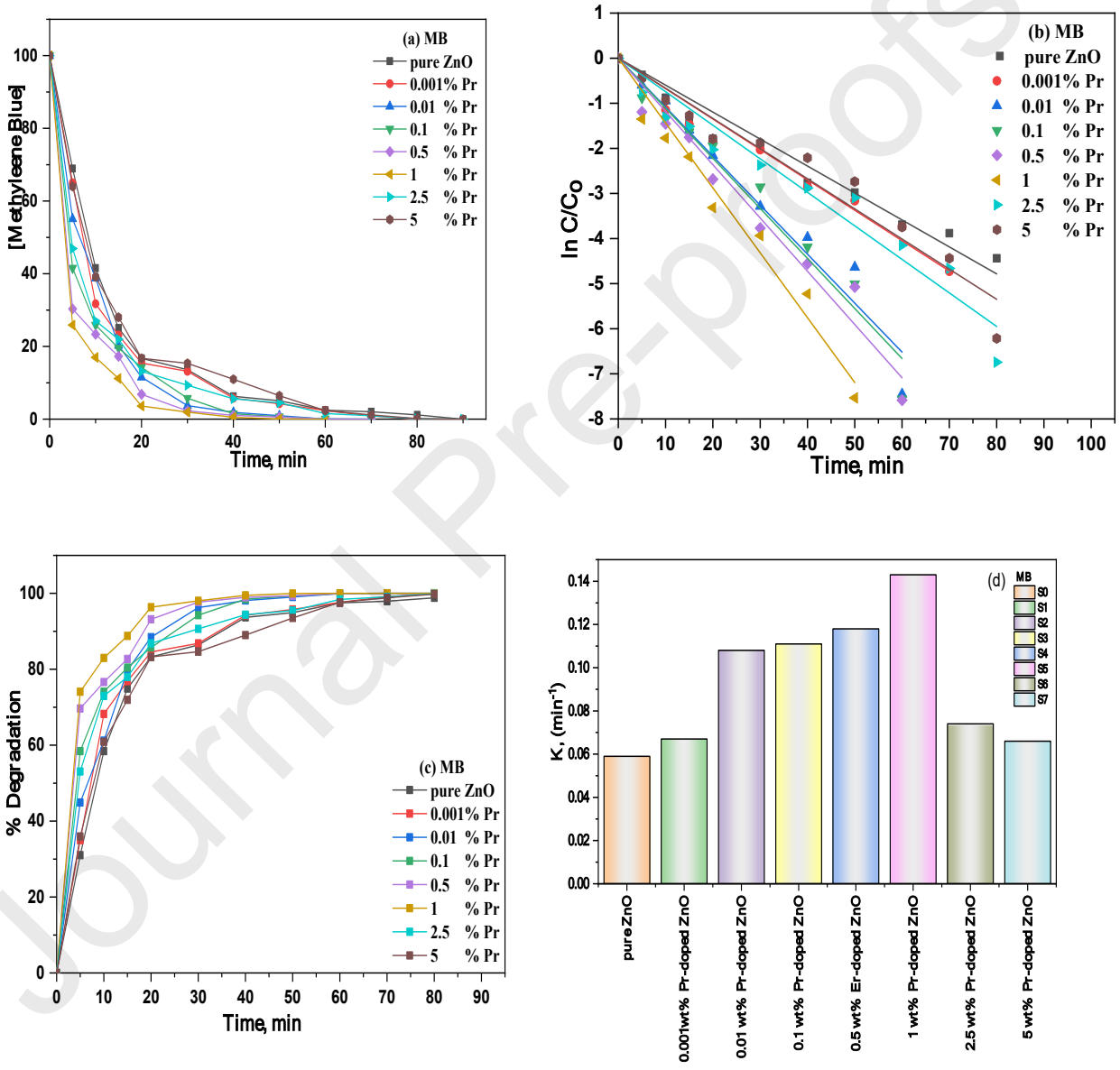

Fig. 7 (a-d). The photodegradation of MB in the presence of pure ZnO and Pr_2O_3-ZnO nanocomposites, with different praseodymium doping concentrations, (a) concentration of MB with time, (b) Kinetic study of photodegradation of MB, (c) % degradation of MB versus Time, (d) Photodegradation rate constant of MB versus all prepared samples.

The rate of degradation increases with the Pr-doping until it reaches a maximum of 1 g Pr-doping (S5); then, it decreases. The efficiency of phenol photodegradation as a function of operating parameters is shown in the photocatalytic degradation % of MB using the synthesized NPs as illustrated in Fig. 7 (c).

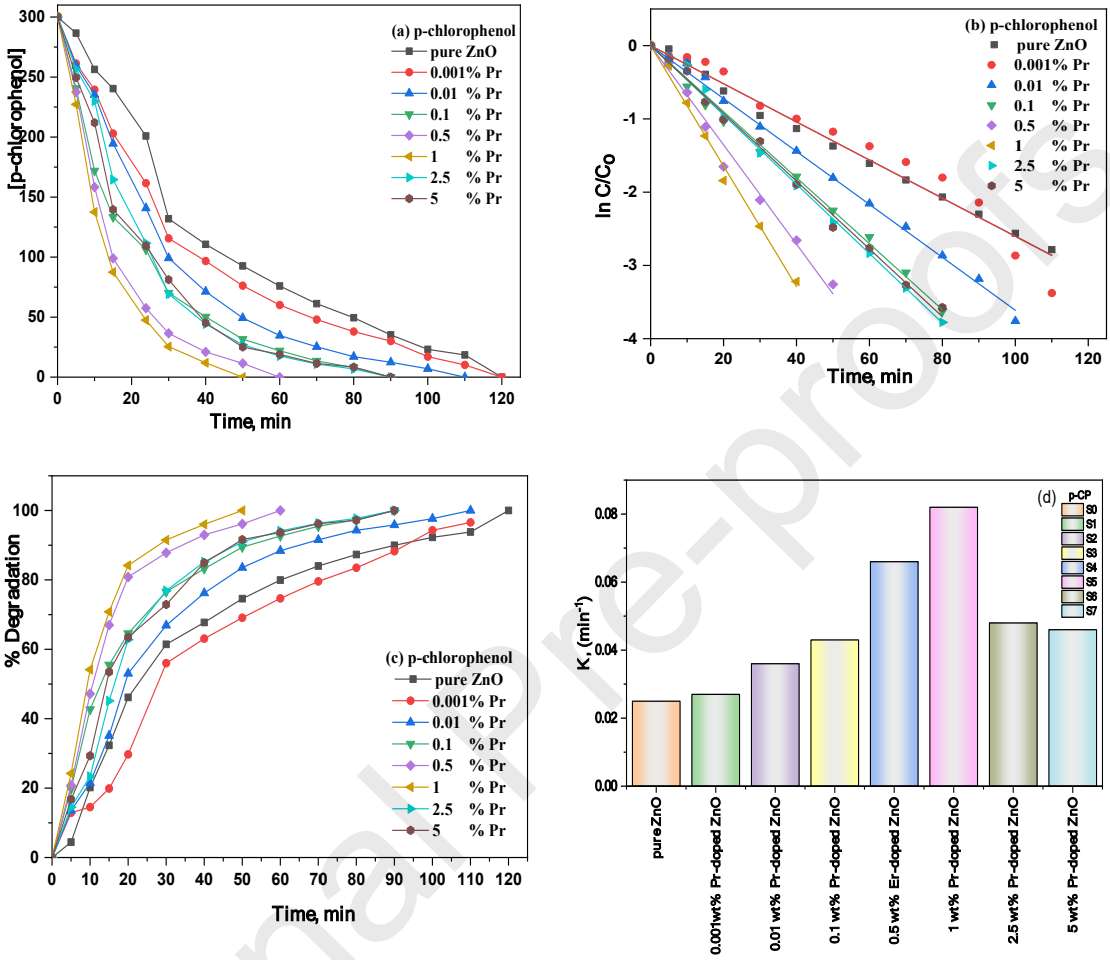

Figs. 7* (a-d). The photodegradation of p-CP in the presence of pure ZnO and Pr_2O_3-ZnO nanocomposites, with different praseodymium doping concentrations, (a) concentration of p-CP with time, (b) Kinetic study of photodegradation of p-CP, (c) % degradation of p-CP versus Time, and (d) Photodegradation rate constant of p-CP versus all prepared samples.

3.4.2. Effect of [H_2O_2].

The primary oxidants such as H_2O_2 superoxide anion radicals, hydroxyl radicals are strong, nonselective oxidants capable of initiating a series of oxidative degradation reactions of organic molecules. Oxidation of organic compounds proceeds through several free radical reactions, producing many intermediates. In exchange, they undergo oxidative cleavage, leading eventually to carbon dioxide, water, and inorganic ions [37]. The effect of H_2O_2 has been illustrated through the photodegradation of MB, and p-CP has been studied. The amount

of H_2O_2 was varied under the same conditions of the photodegradation process with the reaction rates. MB and p-CP photocatalytic degradation have been studied at different H_2O_2 concentrations, as illustrated in Fig. (8&8*), respectively. The degradation rate constant elevated with rising H_2O_2 concentration. H_2O_2 increased linearly from 10^{-6} M up to 10^{-2} M, while the rate of degradation increased till reach the maximum at 10^{-3} M. The values 0.21 and 0.17 min^{-1} are the rate constant for degradation of MB and p-CP, respectively.

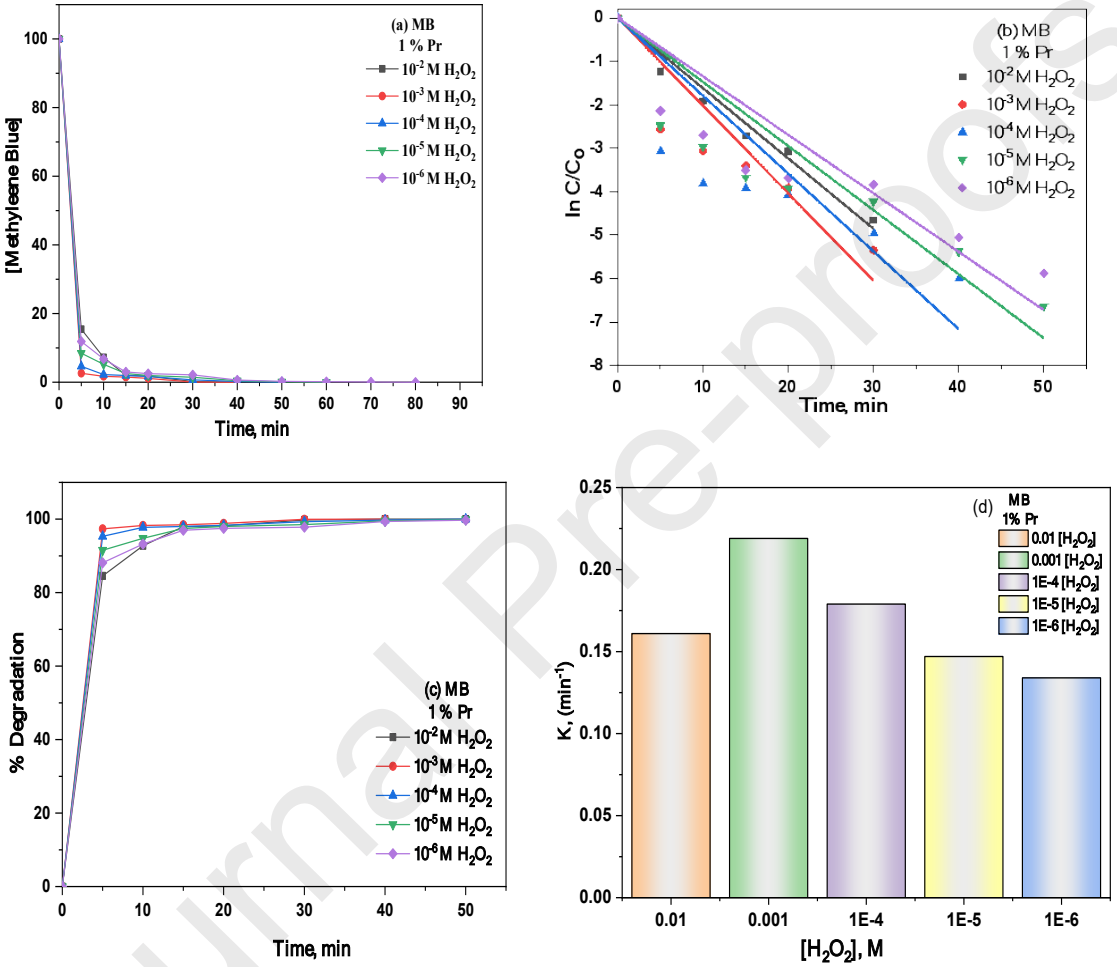

Figs. 8 (a-d). photodegradation of MB in presence of 1% Pr_2O_3-ZnO and different concentrations of H_2O_2, (a) concentration of MB with time, (b) Kinetic study of photodegradation of MB, (c) % degradation of MB versus Time, (d) Photodegradation rate constant of MB versus different concentrations of H_2O_2.

The increase in hydroxyl radical concentration was due to the higher reaction rates following the addition of peroxide. Hydrogen (·H) and hydroxyl radicals (·OH) are generated by light illumination. Consequently, it has been observed that ·OH was generated during light irradiation causes the photodegradation of MB and p-CP [38]. The ·OH oxidizes MB and p-

CP. Consequently, ·OH oxidizes all the obtained produced intermediate species. While on the other side, raising the ·OH concentration can be recombined to H_2O_2. The proper addition of hydrogen peroxide could, therefore, speed up the rate of photodegradation. However, to preserve the hydrogen peroxide's effectiveness, it was crucial to find a suitable dose of hydrogen peroxide based on the form and concentration of the contaminants.

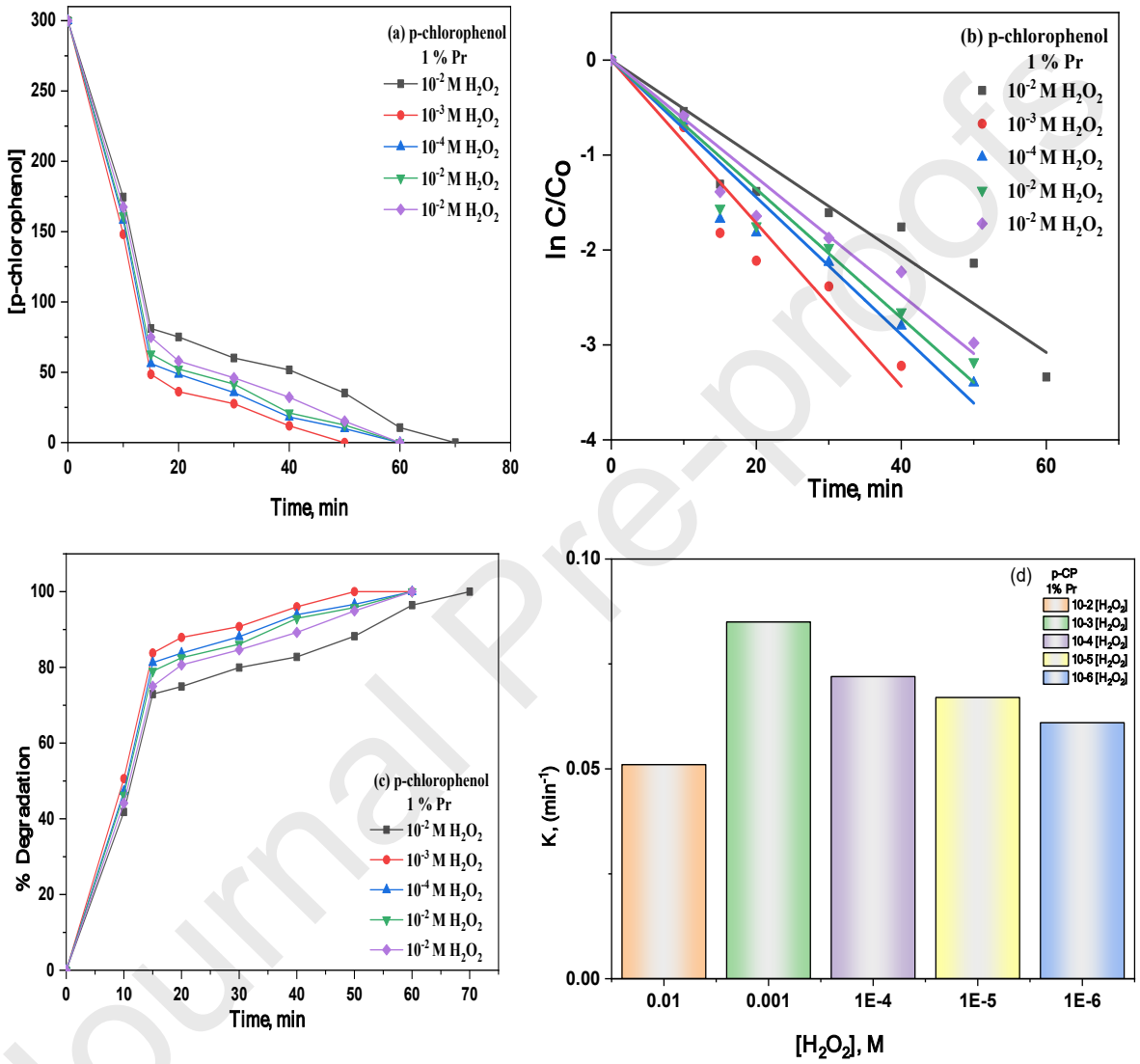

Figs.8* (a-d). photodegradation of p-CP in the presence of 1% Pr_2O_3-ZnO and different concentrations of H_2O_2, (a) concentration of p-CP with time, (b) Kinetic study of photodegradation of p-CP, (c) % degradation of p-CP versus Time, (d) Photodegradation rate constant of p-CP versus different concentrations of H_2O_2.

3.4.3. Influence of pH.

Wastewater containing organic pollutants is discharged at various pH levels so that the function of pH in the organic pollutants' photodegradation must be examined. To investigate

the effect of pH on degradation efficiency, experiments were conducted at various pH values, ranging from 2 to 10 at the same photocatalytic conditions. The pH will be adjusted by adding the proper concentrations of HCl and NaOH to reach the target pH's (2, 4, 6, 8, and 10). Fig. (9&9*) showed the photodegradation efficiency of MB and p-CP, respectively, in terms of pH. The degradation efficiency decreased as pH rises, showing a maximum degradation rate at pH = 4. The photodegradation of dyes and compounds has also been reported to have similar behavior [39]. Because of its various functions, the analysis of pH influences the photocatalytic performance is not straightforward. The pH changes strongly affected the rate of degradation where the highest rate has been noted with pH = 2.

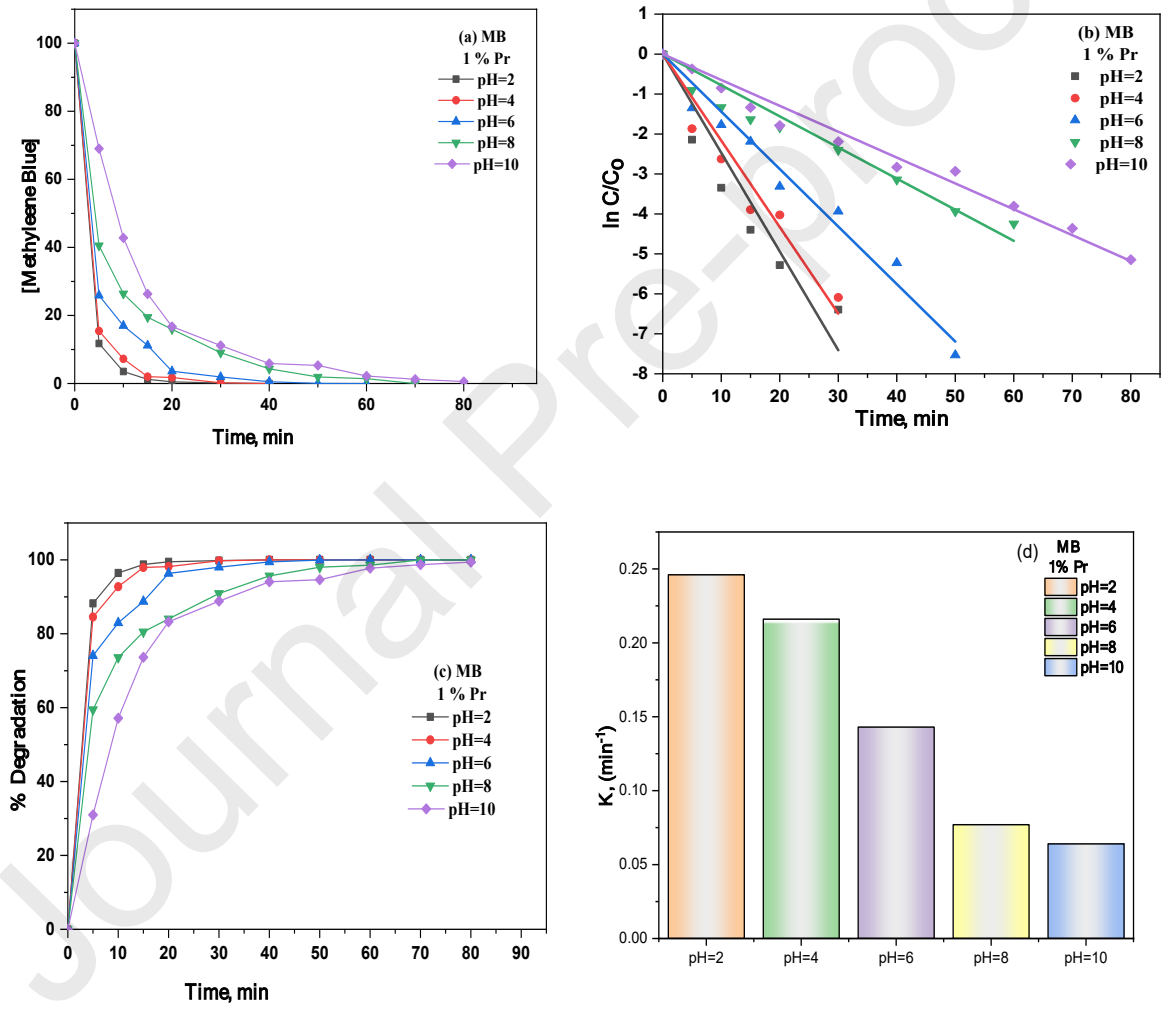

Figs. 9 (a-d). photodegradation of MB in the presence of 1% Pr_2O_3-ZnO and different pHs, (a) concentration of MB with time, (b) Kinetic study of photodegradation of MB, (c) % degradation of MB versus Time, (d) Photodegradation rate constant of MB versus different pHs.

The obtained data showed that the degradation rate is faster at the higher acidic, which may be explained as at higher pH = 10, both organic molecules and catalyst surface are negatively charged, increasing the repulsive force between them, diminishing the adsorption degradation rate. The detailed results suggest that *K* was the strongest for MB and p-CP photodegradation at pH = 2 equal (*K* = 20.5 x 10^{-2} min^{-1} and 7.9 x 10^{-2} min^{-1}), respectively, while at pH 4-8, it had virtually equal kinetic constants of (*K* = 13.0 x 10^{-2} min^{-1}). However, at pH = 10 (*K* = 6.0 x 10−2 min−1), it was significantly reduced. The first deprotonation happens at pH = 8, and the second occurs at pH = 10, based on the *pKa* value of the organic compounds.

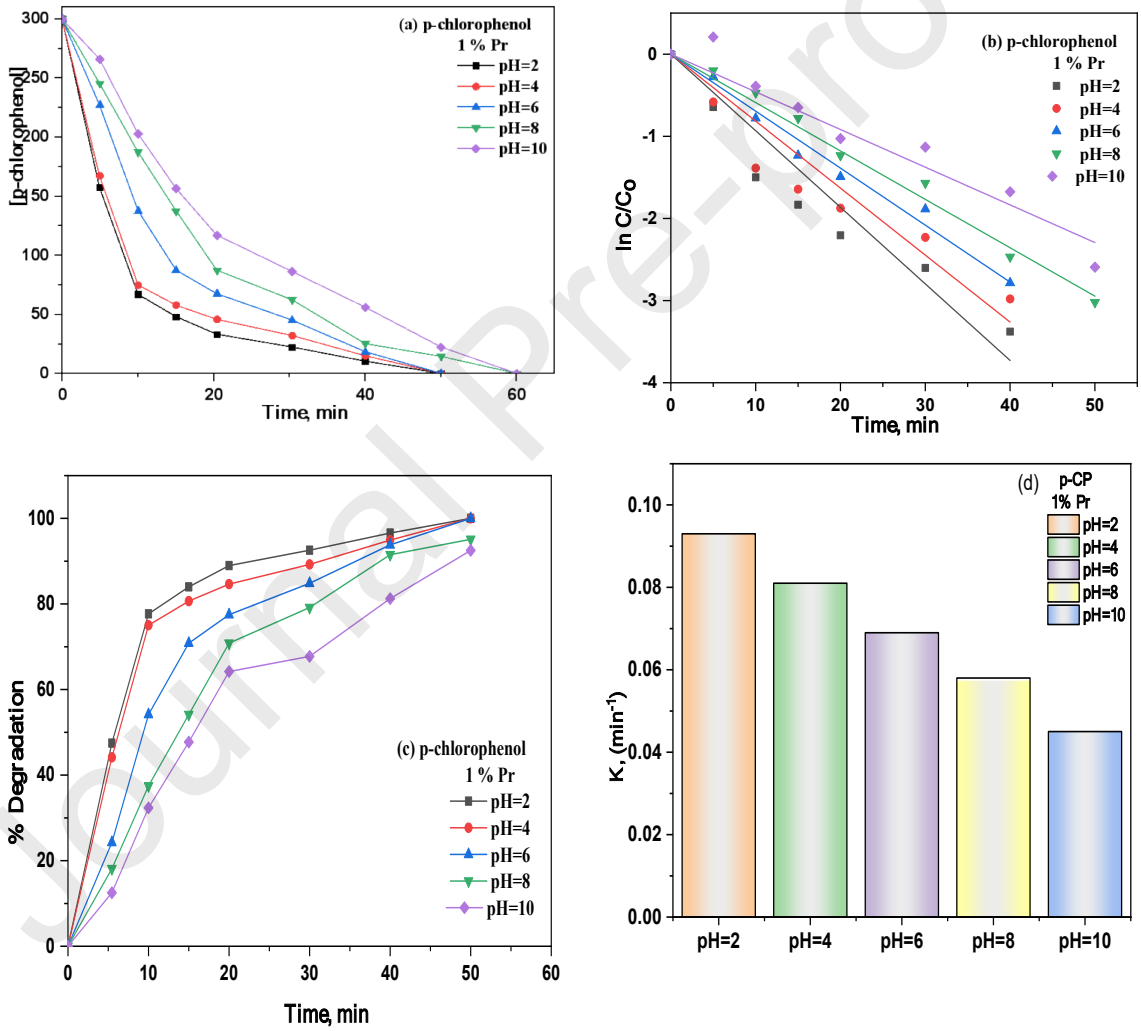

Figs. 9* (a-d). The photodegradation of p-CP in the presence of 1% Pr_2O_3-ZnO and pHs, (a) concentration of p-CP with time, (b) Kinetic study of photodegradation of p-CP, (c) % degradation of p-CP versus Time, (d) Photodegradation rate constant of MB versus different pHs.

4. Conclusion

In this current research, the influence of the praseodymium (Pr) as the dopant in the host ZnO nanoparticles' properties, combined competently in nanostructured powder, were successfully synthesized and studied in detail. The combustion technique, low cost, eco-friendly, high yield, and simple procedure were used to synthesized Pr_2O_3-ZnO nanostructured samples with different doping ratios of Pr-ions. The prepared Pr_2O_3-ZnO nanostructures demonstrated great enhancements in the nanostructure, morphology, dielectric behavior and AC electrical conductivity, optical diffused reflectance, absorption index, optical energy bandgaps, and photocatalytic behaviors are comparing to properties of the host ZnO nanoparticles. The XRD and SEM analysis confirm the synthesized Pr_2O_3-ZnO nanocomposites' polycrystalline structure. The optical study discloses that the praseodymium (Pr) reduces both the direct and indirect optical energy bandgaps of the pure ZnO nanoparticles as the Pr-doping ratio increases. The Pr-doped ZnO showed high photocatalytic degradation performance for MB and p-CP under visible light illumination. The effect of the medium's pH, the concentration of Pr-ions, and concentration in H_2O_2 on the photocatalytic reaction were studied. With Pr-doping ratios increased; the potency of the photocatalytic degradation increased. The 1g of Pr^{3+}-doped ZnO (S5) was an ideal photocatalyst due to 100% degradation of p-chlorophenol and Methylene Blue solutions. The proposed Pr_2O_3-ZnO nanocomposites are amazing candidates, gain more attention to be applied in various critical practical applications, including in electronic/optoelectronic devices, wastewater treatments, photocatalytic, and electrocatalytic removal of toxic chemicals in the water.

References

[1] Y.-Z. Ren, Z.-L. Wu, M. Franke et al., "Sonoelectrochemical degradation of phenol in aqueous solutions," Ultrasonics Sonochemistry, vol. 20, no. 2, pp. 715–721, 2013.

[2] S.M. Lam, J.C. Sin, A.Z. Abdullah, A.R. Mohamed, Degradation of wastewaters containing organic dyes photocatalysed by zinc oxide: a review, Desalination and Water Treatment, 41 (2012) 131-169.

[3] N. Daneshvar, D. Salari, A.R. Khataee, Photocatalytic degradation of azo dye acid red 14 in water on ZnO as an alternative catalyst to TiO_2, Journal of Photochemistry and Photobiology A: Chemistry, 162 (2004) 317-322.

[4] B. Neppolian, A. Bruno, C.L. Bianchi, M. Ashokkumar, Graphene oxide based Pt–TiO_2 photocatalyst: Ultrasound assisted synthesis, characterization and catalytic efficiency, Ultrasonics Sonochemistry, 19 (2012) 9-15.

[5] X. Jin, J. Gao, J. Zha et al., "A tiered ecological risk assessment of three chlorophenols in Chinese surface waters," Environmental Science and Pollution Research, vol. 19, no. 5, pp. 1544–1554, 2012.

[6] Khataee A, Karimi A, Arefi-Oskoui S, Darvishi Cheshmeh Soltani R, Hanifehpour Y, Soltani B and Joo S W 2015 Ultrasonic Sonochem. 22 371

[7] Ong C B, Ng L Y and Mohammad A W 2018 Renewable Sustainable Energy Rev. 81536

[8] Zhang J, Wang Q, Wang L H, Li X A and Huang W 2015 Nanoscale 7 10391

[9] L. Song, C. Chen, S. Zhang, Q. Wei, Sonocatalytic degradation of amaranth catalyzed by La^{3+} doped TiO_2 under ultrasonic irradiation, Ultrasonics Sonochemistry, 18 (2011) 1057 1061.

[10] R. Darvishi Cheshmeh Soltani, A. Rezaee, A.R. Khataee, M. Safari, Photocatalytic process by immobilized carbon black/ZnO nanocomposite for dye removal from the aqueous medium: Optimization by response surface methodology, Journal of Industrial and Engineering Chemistry.

[11] A.R. Khataee, R. Darvishi Cheshmeh Soltani, Y. Hanifehpour, M. Safarpour, H. Gholipour Ranjbar, S.W. Joo, Synthesis and characterization of dysprosium-doped ZnO nanoparticles for photocatalysis of a textile dye under visible light irradiation, Industrial & Engineering Chemistry Research, 53 (2014) 1924-1932.

[12] S.J. Pearton, D.P. Norton, K. Ip, Y.W. Heo, T. Steiner, Prog. Mater. Sci., 50 (2005) 293.

[13] A. B. Patil, K. R. Patil, and S. K. Pardeshi, "Ecofriendly synthesis and solar photocatalytic activity of S-doped ZnO," Journal of Hazardous Materials, vol. 183, no. 1–3, pp. 315–323, 2010.

[14] X. Jia, H. Fan, M. Afzaal, X. Wu, and P. O'brien, "Solid state synthesis of tin-doped ZnO at room temperature: characterization and its enhanced gas sensing and photocatalytic properties," Journal of Hazardous Materials, vol. 193, pp. 194–199, 2011.

[15] S.N. Nam, S.K. Han, J.W. Kang, H. Choi, Kinetics and mechanisms of the sonolytic destruction of non-volatile organic compounds: investigation of the sonochemical reaction zone using several OH monitoring techniques, Ultrasonics Sonochemistry, 10 (2003) 139147.

[16] Venkatesan, D., Deepan, D., Velavan, M., Sankar, R., Jayavel, R., & Dhanasekaran, R. (2010, February). Preparation and characterization of rare-earth (Pr, Nd) doped ZnO nanoparticles. In *2010 International Conference on Nanoscience and Nanotechnology* (pp. 343-347). IEEE.

[17] K.-S. Yu, J.-Y. Shi, Z.-L. Zhang, Y.-M. Liang, and W. Liu, Synthesis, characterization, and photocatalysis of ZnO and Er-doped ZnO. J. Nanomater. 2013, 372951 (2013).

[18] L. Zhang, Y. Yang, R. Fan, J. Yu, L. Li, Improving the efficiency of ZnO-based dye sensitized solar cells by Pr and N co-doping, Journal of Materials Chemistry A, 1 (2013) 12066-12073.

[19] W.D. Callister, Materials science and engineering: An introduction, force ed., John Wiley & Sons, New York, 1997.

[20] P. Banerjee, S. Chakrabarti, S. Maitra, B.K. Dutta, Zinc oxide nano-particles – Sonochemical synthesis, characterization, and application for photo-remediation of heavy metal, Ultrasonics Sonochemistry, 19 (2012) 85-93.

[21] K. SowriBabun, A. Ramachandra Reddy, Ch. Sujatha, K. Venugopal Reddy, Effects of precursor, temperature, surface area and excitation wavelength on photoluminescence of ZnO/mesoporous silica nanocomposite, Ceramics International, 2013, 39, 3055-3064.

[22] F. El-Kabbany, S. Taha, M. Hafez, A study of the phase transition of reheated diphenyl carbazide (DPC) by using UV spectroscopy, Spectrochimica Acta Part A: Molecular and Biomolecular Spectroscopy, 128 (2014) 481–488.

[23] V. Kumar, R.G. Singh, N. Singh, A. Kapoor, R.M. Mehra, L.P. Purohit, Synthesis and characterization of aluminum–boron co-doped ZnO nanostructures, Mater. Res. Bull. 48 (2013) 362-366.

[24] E.A. Davis, N.F. Mott, Conduction in non-crystalline systems V. Conductivity, optical absorption and photoconductivity in amorphous semiconductors, Philos. Mag. 22 (1970) 903-922.

[25] Aydın, C., Abd El-sadek, M. S., Zheng, K., Yahia, I. S., & Yakuphanoglu, F. (2013). Synthesis, diffused reflectance, and electrical properties of nanocrystalline Fe-doped ZnO via sol-gel calcination technique. *Optics & Laser Technology*, *48*, 447-452.

[26] Sh.A. Mansour, I.S. Yahia, F. Yakuphanoglu, The electrical conductivity and dielectric properties of C.I. Basic Violet 10, Dyes Pigm. 2010, 87, 144–148.

[28] Maji, P., Pande, P. P., & Choudhary, R. B. (2015). Effect of Zn (NO3)2 filler on the dielectric permittivity and electrical modulus of PMMA. Bulletin of Materials Science, 38(2), 417-424.

[29] L. Murowski and R.J. Barczynski, Dielectric Properties of Transition Metal Oxide Glasses, Journal of Non-Crystalline Solids, Vol. 185, 1995, p. 84.

[31] M. Kobayashi, M. Mizuno, T. Aizawa, M. Hayashi, K. Mirani, "Development of Zinc Oxide Non-Linear Resistors and their Applications to gapless Surge Arrester", Transactions on Power Apparatus and System, 97 (4), (1978) 1149-1158.

[32] Xu, D., He, K., Yu, R. H., Tong, Y., Qi, J. P., Sun, X. J., … Ma, J. (2014). Microstructure and electrical properties of praseodymium oxide doped Bi2O3based ZnO varistor films. Materials Technology, 30(sup1), A24–A28. doi:10.1179/1753555714y.0000000242

[33] C.W.Nahm, EffectofMnO2 addition on microstructure and electrical properties of ZnO–V2O5-based varistor ceramics, Ceramics International 35 (2) (2009) 541–546.

[34] A.K. Jonscher, Dielectric relaxation in solids (Chelsea Dielectrics, London, 1993)

[35] Zhu JF, Luo HJ, Wang F. Effect of doped Pr6O11 on the properties of ZnO–Bi2O3 system varistors. J Inorg Mater 2006, 21: 381–386.

[36] M. Shekofteh-Gohari, A. Habibi-Yangjeh, M. Abitorabi, A. Rouhi, Magnetically separable nanocomposites based on ZnO and their applications in photocatalytic processes: a review, Crit. Rev. Environ. Sci. Technol. 48 (2018) 806–857.

[37] Y. Liu, S. Shen, J. Zhang, W. Zhong, X. Huang, Cu2−xSe/CdS composite photocatalyst with enhanced visible light photocatalysis activity, Appl. Surf. Sci. 478 (2019) 762–769.

[38] Zyoud A, Dwikat M, Al-Shakhshir S, Ateeq S, Shteiwi J, Zu'bi A, Helal MH, Campet G, Park D, Kwon H (2016) Natural dye-sensitized ZnO nano-particles as photo-catalysts in complete degradation of E. coli bacteria and their organic content. J Photochem Photobiol A: Chem 328:207–216

[39] Bazrafshan E, Amirian P, Mahvi A, Ansari-moghaddam A (2016) Application of adsorption process for phenolic compounds removal from aqueous environments: a systematic review. Glob NEST J 18:146–163

[40] Shirin Ghattavi, Alireza Nezamzadeh-Ejhieh, A visible light driven AgBr/g-C3N4 photocatalyst composite in methyl orange photodegradation: Focus on photoluminescence, mole ratio, synthesis method of g-C3N4 and scavengers, Composites Part B 183 (2020) 107712

Highlights

- The combustion as a simple, efficient, inexpensive, and environmental method was used to prepare the samples of undoped and several concentrations of praseodymium-doped zinc oxide (Pr_2O_3- ZnO) nanoparticles ranged from 0.001 g to 5 g.
- The structure, morphology, and chemical bonding were investigated by X-ray diffraction (XRD), scanning electron microscopy (SEM), and Fourier transforms infrared spectroscopy (FT-IR), respectively, of the prepared Pr_2O_3-ZnO photocatalysts.
- Furthermore, the optical features have been investigated via UV-Vis diffused reflectance spectroscopy (DR), and AC electrical conductivity was studied to investigate the Pr^{3+}-nanoparticles' influence on the optical characteristics, energy bandgaps, of all proposed Pr_2O_3-ZnO nanostructured samples.
- The addition of Pr^{3+} dopants decreases the energy bandgap slightly and confines the photogenerated electron-hole recombination.
- The studied Pr_2O_3-ZnO nano-samples have been applied in photocatalytic degradation of methylene blue (MB) as an example for organic dyes and p-chlorophenol (p-CP) as a type of colorless phenolic compounds under visible light irradiation. The influence of Pr^{3+}-concentration, H_2O_2 concentration, and pH of the medium on the photocatalytic reaction have been studied.
- As the praseodymium doping ratios increased; the photocatalytic efficiency increased. After the addition of moderate Pr^{3+}-doping, further generation of hydroxyl radicals over ZnO. For 1% Pr^{3+}-ZnO, the optimal photocatalyst is a degradation of 100% of p-chlorophenol and methylene blue solutions.
- The prepared Pr_2O_3-ZnO nanostructured samples are amazing, promising candidates in novel potential nano-applications for wide-ranged from varistors, wastewater treatments, biomedical and photocatalytic degradation for phenol and organic dyes to different environmental fields.